Chinese Journal of Catalysis 42 (2021) 2296–2305

available at www.sciencedirect.com

journal homepage: www.sciencedirect.com/journal/chinese-journal-of-catalysis

Article

# Electrocatalytic generation of hydrogen peroxide on cobalt nanoparticles embedded in nitrogen-doped carbon

Basil Sabri Rawah [a,b], Wenzhen Li [a,*]

[a] *Chemical and Biological Engineering Department, Biorenewables Research Laboratory, Iowa State University, Ames, IA 50011, USA*
[b] *Chemical and Biological Engineering Department, University of Jeddah, Jeddah 23890, Saudi Arabia*

ARTICLE INFO

*Article history:*
Received 14 January 2021
Accepted 6 March 2021
Available online 10 September 2021

*Keywords:*
Hydrogen peroxide
Two-electron oxygen reduction
Carbon catalyst
Electrocatalysis

ABSTRACT

Electrocatalytic reduction of oxygen is a growing synthetic technique for the sustainable production of hydrogen peroxide ($H_2O_2$). The current challenges concern seeking low-cost, highly active, and selective electrocatalysts. Cobalt-nitrogen-doped carbon containing catalytically active cobalt-nitrogen ($Co\text{-}N_x$) sites is an emerging class of materials that can promote the electrochemical generation of $H_2O_2$. Here, we report a straightforward method for the preparation of cobalt-nitrogen-doped carbon composed of a number of $Co\text{-}N_x$ moieties using low-energy dry-state ball milling, followed by controlled pyrolysis. This scalable method uses inexpensive materials containing cobalt acetate, 2-methylimidazole, and Ketjenblack EC-600JD as the metal, nitrogen, and carbon precursors, respectively. Electrochemical measurements in an acidic medium show the present material exhibits a significant increase in the oxygen reduction reaction current density, accompanied by shifting the onset potential into the positive direction. The current catalyst has also demonstrated an approximate 90 % selectivity towards $H_2O_2$ across a wide range of potential. The $H_2O_2$ production rate, as measured by $H_2O_2$ bulk electrolysis, has reached 100 mmol $g_{cat.}^{-1}$ $h^{-1}$ with high $H_2O_2$ faradaic efficiency close to 85% (for 2 h at 0.3 V *vs.* RHE). Lastly, the catalyst durability has been tested (for 6 h at 0.3 V *vs.* RHE). The catalyst has shown relatively consistent performance, while the overall faradic efficiency reaches approximate 85% throughout the test cycle indicating the promising catalyst durability for practical applications. The formed $Co\text{-}N_x$ moieties, along with other parameters, including the acidic environment and the applied potential, likely are the primary reasons for such high activity and selectivity to $H_2O_2$ production.



## 1. Introduction

Hydrogen peroxide ($H_2O_2$) is a promising oxidant for green and sustainable chemistry, also considered a valuable product for the industry [1]. The industrial $H_2O_2$ synthesis relies primarily on a multi-step anthraquinone oxidation (AO) process. Despite its large-scale and high-purity production, the process still faces major sustainability and safety issues in terms of energy use, industrial waste management, as well as storage and transport costs [2]. Another route that has been studied is the direct synthesis of $H_2O_2$ from molecular oxygen and hydrogen. This alternative method, however, faces challenges such as operating potentially explosive mixtures of $H_2/O_2$, inevitable side reactions, and the need of a platinum-based metal catalyst [3]. Therefore, novel, sustainable, safe, and ecofriendly routes to $H_2O_2$ generation are highly needed.

Employing electrochemical processes for chemicals synthesis has become an attractive route mostly for its sustainability

* Corresponding author. Tel: +1-515-294-4582; E-mail: wzli@iastate.edu
DOI: 10.1016/S1872-2067(21)63804-4 | http://www.sciencedirect.com/journal/chinese-journal-of-catalysis | Chin. J. Catal., Vol. 42, No. 12, December 2021

and efficiency [4]. A major focus is on the electrocatalytic oxygen reduction reaction (ORR) to synthesize hydrogen peroxide. At the cathode of an electrochemical cell, oxygen could be either reduced to $H_2O$ or $H_2O_2$ through a competing four- or two-electron transfer pathway, respectively.

The four-electron electrochemical reduction of $O_2$ to $H_2O$ proceeds in an acidic electrolyte, according to Eq. (1). Or, the two-electron partial reduction of $O_2$ to $H_2O_2$ occurs primarily by Eq. (2)

$$O_2 + 4H^+ + 4e^- \rightarrow 2H_2O \qquad E^0 = 1.23\ V \qquad (1)$$

$$O_2 + 2H^+ + 2e^- \rightarrow H_2O_2 \qquad E^0 = 0.7\ V \qquad (2)$$

The four-electron pathway seemed to have gained considerable interest for various energy conversion or storage purposes, like those for fuel cells and metal-air batteries [5]. Much work is currently focused on developing advanced catalysts to promote the four-electron route between the $O_2$ and $H_2O$ to improve the devices' energy conversion efficiency. On the other hand, a highly selective two-electron reduction into hydrogen peroxide may also be desirable, as it could cogenerate a valuable commodity and electricity [6].

This $H_2O_2$ electrosynthesis route prevents the danger of explosion by feeding the $H_2$ and $O_2$ into two distinct compartments separated by an ion-exchange membrane. Furthermore, generating $H_2O_2$ in a fuel cell configuration using $H_2$ oxidation at the anode would be an efficient process by cogenerating electrical energy during the reaction. Alternatively, $H_2$ molecules can be removed entirely by using an electrolytic cell. In this mode, water will substitute $H_2$ as a proton formation source, and oxygen evolves at the anode [7]. Besides the scalability of electrochemical devices, this approach allows in situ generations of $H_2O_2$ from renewable energy sources, thereby reducing energy consumption as well as storage and transport costs.

The performance of electrochemical devices to generate $H_2O_2$ is often linked to the catalyst activity at the electrode. A successful electrocatalyst needs to be highly selective and active, as well as ensure high levels of stability and durability for long-term operation [8]. Currently, state-of-the-art catalysts contain precious platinum or palladium metals, which are atomically distributed on the support matrix. They rely on isolated sites of reactive atoms, Pt or Pd, surrounded by more inert atoms, N, S, and C or through the use of inactive metals such as Hg to produce metal alloys (Pt-Hg, Pd-Hg and Ag-Hg) [4,8,9]. However, the complex synthesis and associated high cost of the precious-metals and, more importantly, the possible agglomeration of Pt atoms, Pt cluster formation, favoring the four-electron pathway are crucial obstacles in a practical application of electrochemical $H_2O_2$ synthesis [10].

Several cathode catalysts have been proposed, and carbon materials are considered as promising alternative ORR catalysts for $H_2O_2$ electrochemical production, apparently due to the use of abundant precursors, high selectivity, acceptable stability, and simple preparation [11–13]. The incorporation of heteroatom dopants, more specifically, nitrogen atoms can further improve the $H_2O_2$ selectivity, which can be attributed to the special electronic properties arise from the conjugation between the nitrogen-lone-pair electrons orbitals and the graphitic structure [14].

Despite the achieved performance, nitrogen-doped carbons have concerns associated with their very high ORR overpotential resulting in low energy efficiency to produce $H_2O_2$ [15–17]. Much effort has been made to enhance the very low ORR activity of pure nitrogen-doped, particularly by incorporating specific transition metals into its structure, creating M-$N_x$ reactive sites that can improve catalytic activity.

Among the various transition metal-containing $N_x$ chelate macrocycles, Co-porphyrins and -phthalocyanins with well-defined Co-$N_x$ active sites showed considerable activity and selectivity for $H_2O_2$ production [18–20]. However, the complicated syntheses of Co-$N_x$ macrocycles, plus the high cost of some key precursors, have restrained their practical use for peroxide production [21,22]. In addition, it is not clear if Co nanoparticles (Co-NPs) exist in the catalytic system, and the contributions of Co-NP and Co-$N_x$ to the $H_2O_2$ synthesis from partial oxygen reduction need be clarified. It, therefore, seems highly desirable to develop a simple, affordable, and scalable approach for Co-N-C synthesis that can selectively perform ORR to produce $H_2O_2$.

Herein, we reported a straightforward preparation of cobalt-N-doped carbon (Co-N-KB), including some Co-$N_x$ moieties developed on the catalyst matrix using dry-state low energy ball milling, preceded by controlled pyrolysis. This scalable procedure used low-cost materials containing cobalt acetate as the metal precursor and 2-methylimidazole as nitrogen sources and Ketjenblack EC-600JD carbon (KB) as the catalyst support. The Co-N-KB exhibited outstanding electrocatalytic behavior to reduce oxygen to $H_2O_2$ in acidic medium. Rotating ring-disk electrode (RRDE) measurements were employed to investigate the catalyst activity and selectivity towards $H_2O_2$ generation from $O_2$ reduction. Moreover, the Co-N-KB electrocatalytic performance was compared with nitrogen doped carbon (N-KB), pristine carbon (KB) in order to separately examine the role of the embedded Co and N dopants on the catalytic behavior. Furthermore, a comparative analysis was carried out to explore the role of the embedded Co-NPs in $H_2O_2$ synthesis by evaluating the electrocatalytic activity of Co-N-KB toward $H_2O_2$ before and after the acid treatment in combination with testing the ORR activity of commercial Co-NPs under the same experimental conditions. Finally, the Co-N-KB catalyst was tested in a batch electrolysis cell to evaluate its capability and durability for practical $H_2O_2$ production.

## 2. Experimental

### 2.1. Material preparation

In a typical procedure, approximately 250 mg of Ketjenblack EC-600JD, KB (AkzoNobel), 45 mg of cobalt (II) acetate (Sigma-Aldrich), and 400 mg of 2-methylimidazole (Sigma-Aldrich), the nitrogen source, were added and then mixed *via* a low energy ball milling (CryoMill, Retsch) for 20 min. The purple mixture was pyrolyzed in a tube furnace for 2 h in Ar gas at 850 °C, where this temperature is optimal for gains in N and moderate metal contents [23,24]. The cobalt-nitrogen

doped carbon catalyst (Co-N-KB) was collected without further treatments. The acid-washed sample (Acid-W/Co-N-KB) was further treated in 0.5 M $HClO_4$ at 80 °C for 3 h to remove the most of Co-NPs, as well as unstable cobalt species on the catalyst surface. The sample was then washed with DI water for 3 times, centrifuged, filtered, and overnight dried at 60 °C. For the nitrogen doped carbon (N-KB) sample, the same Co-N-KB procedure was followed, with the exception of adding the cobalt precursor. Finally, commercial Co-NPs (US Research Nanomaterials, Inc.) on N-KB catalyst was prepared by physical mixing of Co-NPs and N-KB without any further treatment.

### 2.2. Material characterization

The structural morphologies of the catalysts were characterized by FEI Quanta 250 scanning electron microscopy (SEM) and 200kV JEOL 2100 transmission electron microscopy (TEM). Powder X-ray diffraction (XRD) patterns were obtained from a Rigaku Ultima IV X-ray diffraction XRD systems with Cu $K_\alpha$ radiation ($\lambda$ = 1.54056 Å), in the range from 15° to 90°. The surface compositions and their corresponding various binding energy peaks were identified by X-ray photoelectron spectroscopy (XPS) with Mg $K_\alpha$ alpha X-ray (1253.6 eV) (Kratos Amicus/ESCA 3400).

### 2.3. Electrocatalytic characterization

The electrochemical measurements were carried out in home-made-three-electrode electrochemical cells connected to a multi-channel potentiostat (Biological) and a rotator (Pine MSR:AFMSR636A). The three-electrode setup consists of a rotating disk electrode (working electrode), coiled platinum (counter electrode), and a silver/silver chloride (Ag/AgCl) reference electrode in an acidic solution of 0.5 M $H_2SO_4$. For the working electrode fabrication, the catalyst ink, a mixture of a dispersed catalyst powder, water, isopropanol, and 5 wt% Nafion (Sigma-Aldrich) solution, was dropped onto the surface of the RRDE (electrode area of 0.19625 $cm^2$) with a catalyst loading of 50 ug $cm^{-2}$. In this study, all electrode potentials were converted to RHE.

The ORR activity of the catalyst was examined *via* linear sweep voltammetry (LSV), which was performed at 5 mV $s^{-1}$ scan rate in $O_2$-saturated electrolyte. Before the ORR measurements, Pt ring electrode of the RRDE was electrochemically cleaned by carrying out multiple CVs between 1.2 and −0.1 $V_{RHE}$ at a scan rate of 20 mV $s^{-1}$ in Ar saturated electrolyte until a stable curve was obtained. Then, the capacitive (non-faradic) current of the RRDE disk was collected *via* LSV between 1.1 and −0.1 $V_{RHE}$ at a scan rate of 5 mV $s^{-1}$ in Ar-saturated 0.5 M $H_2SO_4$ solution. Next, $O_2$ was purged for 30 min to saturate the electrolyte before studying the ORR activity through conducting LSV between 1.1 and −0.1 $V_{RHE}$ at a scan rate of 5 mV $s^{-1}$ and 1600 rpm with a fixed Pt ring potential of 1.2 $V_{RHE}$ to detect the RRDE disk electrode generated $H_2O_2$. The ORR faradic current was corrected *via* subtracting the non-faradic current measured previously *via* LSVs in an Ar-saturated electrolyte.

Based on currents generated on the disk ($I_d$) and the ring ($I_r$). The $H_2O_2$ selectivity and the number of electron transferred ($n$) were calculated using the following equations:

$$H_2O_2\ (\%) = 200I_d/(N\,|I_d| + I_r) \quad (3)$$

$$n = 4I_d/(|I_d| + I_r/N) \quad (4)$$

The collection efficiency ($N$) was experimentally determined to be 18.5%.

#### 2.3.1. Hydrogen peroxide bulk electrolysis

A custom two-compartments Cell (H-Cell) separated by an ion-exchange membrane (Nafion 212) was used to evaluate bulk $H_2O_2$ production. The membrane was pretreated sequentially with 1 M $H_2O_2$ and 1 M $H_2SO_4$ at a temperature of 80 °C for 1 h. Both compartments had 0.5 M $H_2SO_4$ solutions, while the catalyst load was maintained at 100 ug $cm^{-2}$. Prior to the electrochemical measurements, the manual IR compensation (MIR) method was employed to correct the electrolyte resistance. Then, chronoamperometry (CA) technique at 0.2 and 0.3 $V_{RHE}$ was applied in $O_2$ saturated electrolyte stirred at 250 rpm for 2 h.

The catalyst durability was performed at a constant potential of 0.3 $V_{RHE}$ in $O_2$ saturated $H_2SO_4$ for 6 h. The test was conducted in two-hour intervals, with fresh $H_2SO_4$ solution being added to replace the previous solution before the subsequent test.

For quantification of the $H_2O_2$ concentration, samples were initially collected at certain time intervals and then analyzed using the iodide/UV-Vis spectroscopy method. Details of the iodometric spectrophotometry were given elsewhere [25]. The sample of $H_2O_2$ was added to equal amounts of solutions A and B and left to mix for 3 min. Next, the UV-Vis measurements were carried out at 351 nm, and then the hydrogen peroxide concentrations were calculated based on the calibration curve constructed using a standard $H_2O_2$ solution. The Faradic efficiency of $H_2O_2$ was determined using the following equation:

$$H_2O_2\ \text{Faradic efficiency}\ (\%) = 2 \times \frac{VCF}{Q} \quad (5)$$

Where $V$ is the electrolyte volume (L), volume, $C$ is the $H_2O_2$ generated concentration (mol $L^{-1}$), F is the faraday constant (C $mol^{-1}$), and $Q$ is the sum of passed charge (C).

## 3. Results and discussion

### 3.1. Material synthesis

The synthesis procedure of the Co-N-KB catalyst is illustrated in Fig. 1. Briefly, the catalyst, which contains Ketjenblack carbon, EC-600JD (KB) as the catalyst support, 2-methylimidazole for nitrogen doping, and cobalt acetate as the metal precursor for the Co-$N_x$ moieties, was prepared *via* dry state low-energy ball milling and pyrolyzed in Ar gas at 850 °C for 2 h, to achieve the Co-N-KB catalyst without further treatment. Detailed synthesis is presented in the experimental section. It is worth mentioning that, for its high electroconductivity and its BET surface area (~400 $m^2/g$). Ketjenblack was chosen as a carbon support.

### 3.2. Material characterization

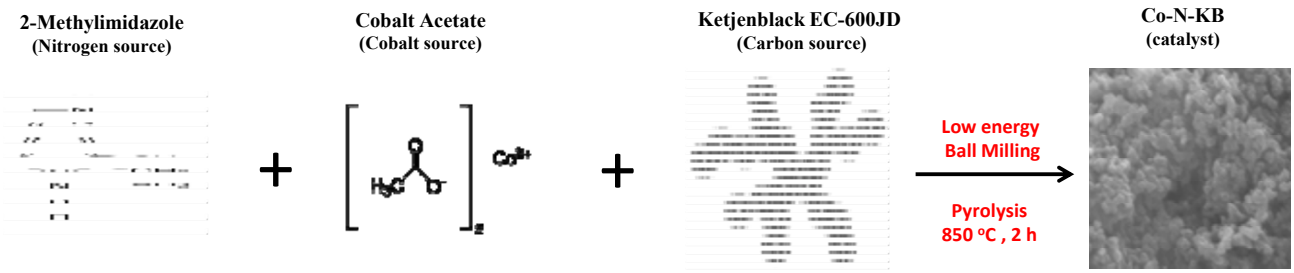


**Fig. 1.** Synthesis scheme of the Co-N-KB catalyst.

The Co-N-KB catalyst structural morphology was examined by SEM and TEM. The SEM images (Figs. 2(a–c)) of Co-N-KB, N-KB, and KB, respectively, demonstrated the presence of similar structures of highly dense carbon aggregates. The SEM results confirmed no morphological changes upon incorporating Co or N doping. Additionally, TEM analysis (Figs. 3(a) and (b) showed that the Co-N-KB catalyst contained Co nanoparticles (Co-NPs) embedded in the N doped carbon matrix, primarily within the 10–25 nm size range. The Co-NPs were rarely aggregated, suggesting a good dispersion in the carbon layer. Furthermore, The HR-TEM image (Fig. 3(c)) showed that the core Co-NP was encapsulated inside the N-doped carbon shell, which may effectively keep the Co-NPs from agglomerating or oxidizing excessively [26,27].

The XRD peaks of the samples (Fig. 4) were also measured. The XRD measurements for Co-N and N-doped samples were very similar to the pristine sample with two prominent broad, amorphous carbon diffraction peaks centered at 24° and 43° [28]. This result suggested no significant structural change during the doping process, and this is in good agreement with the observed SEM images. XRD also detected some metallic Co residuals for the Co-N-KB sample, but no sign of metal oxides was noted.

The surface chemical composition of the Co-N-KB was examined using XPS. Fig. 5 shows a wide-scan XPS survey spectrum with a series of peaks corresponding to C 1*s* (284.4 eV), N 1*s* (398.5 eV), O 1*s* (532.3 eV), and Co 2*p* (780.4 eV). XPS also estimated C, N, O, and Co compositions to be 94.66 at%, 2.11 at%, 2.93 at%, and 0.29 at%, respectively. For N-KB catalyst, XPS spectra confirmed the formation of similar peaks of C 1*s*, N 1*s*, and O 1*s* (except Co 2*p* peak) near the catalyst's surface.

The narrow scan N 1*s* spectrum of Co-N-KB shown in Fig. 6(a) evidences the formation of Co-$N_x$ moieties (398.84 eV), as well pyridinic-N (398.24 eV), pyrrolic-N (400.24 eV), and gra-

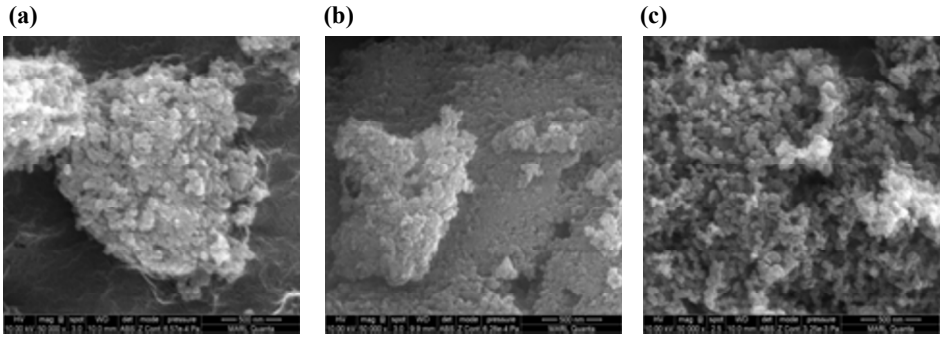


**Fig. 2.** SEM images of Co-N-KB (a), N-KB (b), and KB (c).

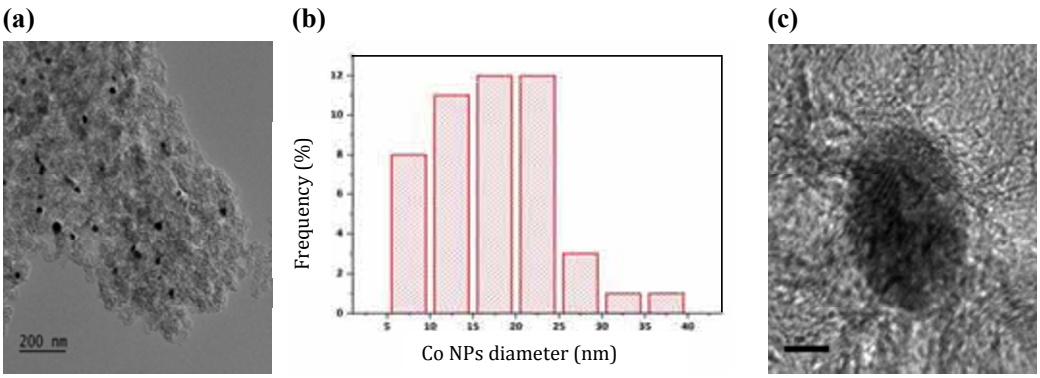


**Fig. 3.** TEM image (a), cobalt nanoparticles particle size distribution calculated from TEM images (b), and HR-TEM image (c) of Co-N-KB catalyst.

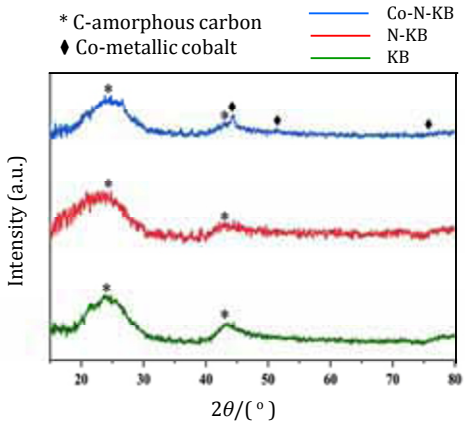


**Fig. 4.** XRD patterns of KB (bottom), N-KB (middle) and Co-N-KB (top) catalysts.

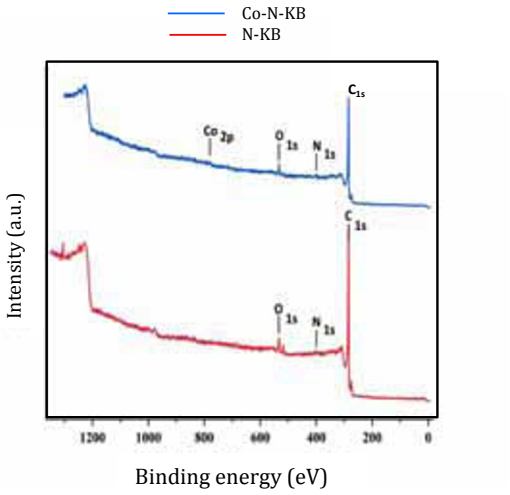


**Fig. 5.** XPS survey spectra of N-KB (bottom) and Co-N-KB (top).

phitic-N (401.34 eV). Table 1 shows the atomic percentages of N species of Co-$N_x$ (25.08 at%), pyridinic-N (32.67 at%), pyrrolic-N (20.87 at%), and graphitic-N (21.39 at%) [29–31].

High-resolution Co $2p_{3/2}$ spectrum in Fig. 6(b) observed two key components corresponding to Co-$N_x$ and CoO, including shake-up (satellite) peaks. The first maximum peak is located at 780.31 eV, consistent with the Co $2p_{3/2}$ binding energy of Co coordinated $N_x$, suggesting the development of Co-$N_x$ active sites on the N-doped carbon framework [32,33]. The second maximum peak centered at 779.21 eV corresponds with the Co $2p_{3/2}$ binding energy of CoO [4]. The $Co^0$ nanoclusters are air-sensitive, and therefore, due to Co NP exposure to ambient air, a thin layer of Co-oxides could be formed [27,34]. XPS has not found a zero-valent Co confirming the encapsulation of Co nanoparticles within the carbon system. Table 2 presents the XPS composition analysis of Co, showing the dominant existence of Co-$N_x$ with (72.98 at%). This result supports the prevalence of Co-$N_x$ moieties near the catalyst surface. The High-resolution XPS spectrum for the Co-N-KB samples confirmed the existence of dense $N_x$ coordinating Co moieties near the surface, which is likely to boost the ORR behavior for $H_2O_2$ [18,35].

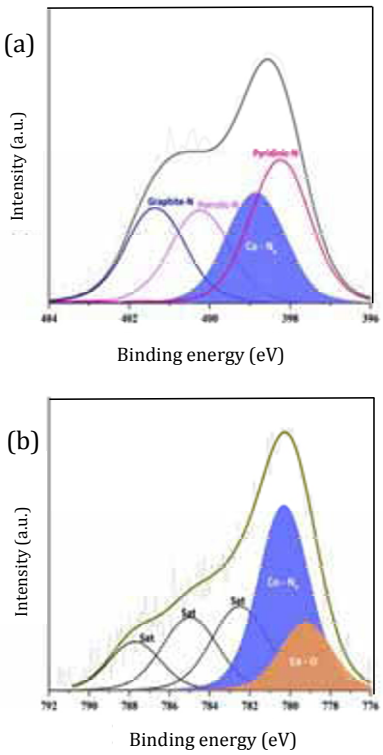


**Fig. 6.** High-resolution XPS spectra of N 1*s* (a) and Co $2P_{3/2}$ (b) of the Co-N-KB catalyst.

### 3.3. *Electrocatalytic analysis*

#### 3.3.1. *$H_2O_2$ selectivity and the number of transferred electrons*

In order to examine the ORR activity, LSV approach was employed to perform a comparative analysis on the Co-N-KB, N-doped-KB, and pristine KB. Fig. 7 plots the disk current density and the ring current of all samples collected from RRDE measurements. With a current density of 0.05 mA $cm^2$, the onset potential of N-doped-KB shifted positively to 0.355 $V_{RHE}$

**Table 1**
Elemental composition of the Co-N-KB catalyst from high-resolution XPS spectra of N 1*s*.

| Catalyst | Binding energy (eV) | Atomic percentage (%) |
|---|---|---|
| Pyridinic-N | 398.24 | 32.67 |
| Co-$N_x$ | 398.84 | 25.08 |
| Pyrrolic-N | 400.24 | 20.87 |
| Graphite-N | 401.34 | 21.39 |

**Table 2**
Elemental composition of the Co-N-KB catalyst from high-resolution XPS spectra of Co $2p_{3/2}$.

| Catalyst | Binding energy (eV) | Atomic percentage (%) |
|---|---|---|
| Co | 778.21 | — |
| CoO | 779.21 | 27.01 |
| Co-$N_x$ | 780.31 | 72.98 |

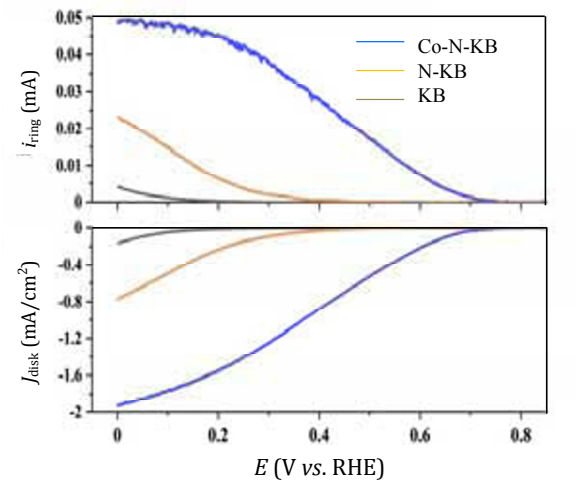


**Fig. 7.** Ring currents measured on the Pt-ring at 1.2 $V_{RHE}$ (top) the disk current density (bottom) of KB, N-KB and Co-N-KB catalysts with the same catalyst loading measured by RRDE at 1600 rpm in $O_2$ saturated 0.5 M $H_2SO_4$.

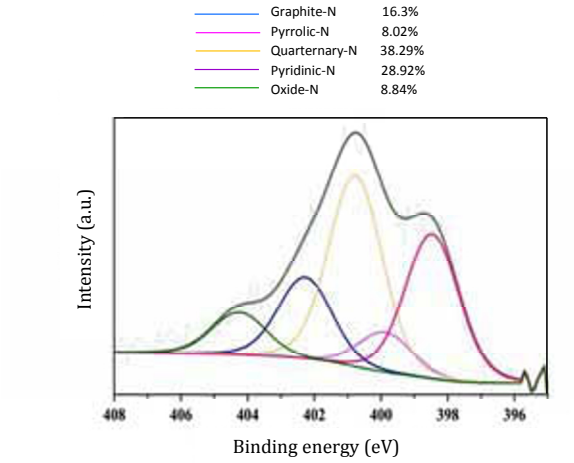


**Fig. 8.** High-resolution XPS spectra of N 1*s* of the N-KB catalyst.

from 0.096 $V_{RHE}$. The N doped sample also improved the current ORR densities, such as the notable increase from 0.163 mA/cm$^2$ to 0.771 mA/cm$^2$ at 0 $V_{RHE}$. The results indicated that the incorporation of heteroatoms, in particular N dopants, improved the ORR activities over the pristine sample. Graphic N and pyridine N formation on the carbon framework (Fig. 8) could serve as active sites enhancing the ORR performance. Some previous studies have reported that pyridinic N could increase the ORR onset potential, while graphitic N could significantly boost the limiting current density [27,36].

Furthermore, simultaneous integration of Co and N further improved the ORR activity, with an onset potential of 0.58 $V_{RHE}$ and a current ORR density of 1.93 mA/cm$^2$ at 0 $V_{RHE}$. The Co-N-KB catalyst outperformed the metal-free N doped sample by positively shifting the onset potential with 255 mV as well as increasing current density around 2.5 folds.

In addition to the adequate ORR current density and improvement in the onset potential, the Co-N-KB catalyst showed by far the highest ring current, 0.049 mA at 0 $V_{RHE}$, thereby demonstrating a good balance between ORR catalytic activity and high selectivity towards the generation of $H_2O_2$.

To further explore the ORR catalytic pathway toward $H_2O_2$ generation and its associated reaction mechanism, measurements of $H_2O_2$ selectivity and transferred electron number were performed on Co-N-KB and N-KB samples. Figs. 9(a) and (b) shows the $H_2O_2$ selectivity and transferred electron number profiles for Co-N-KB and N-KB, respectively.

The N dopant sample exhibited higher $H_2O_2$ selectivity as applied potential increased. The result implies that the N-KB catalyst experienced high ORR overpotential, narrowing the selectivity window at a more negative potential. Conversely, the Co-N-KB catalyst exhibited higher $H_2O_2$ selectivity with the applied potential decreased, implying the Co incorporation could lower the ORR overpotential, likely promoting the $H_2O_2$ generation at more positive potentials. The number of electrons transferred showed an opposite trend indicating that the Co-N-KB catalyst favoring the two electrons ORR pathway for $H_2O_2$ production as the potential lowered [37].

To better understand Co-integration, the $H_2O_2$ selectivity

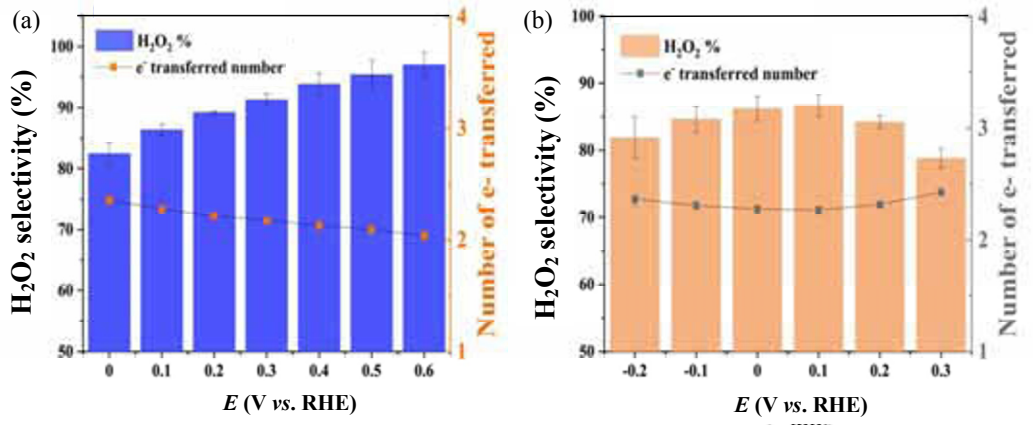


**Fig. 9.** $H_2O_2$ selectivity and the number of transferred electrons (*n*) profiles of Co-N-KB (a) and N-KB (b) catalysts with the same catalyst loading measured by RRDE at 1600 rpm in $O_2$ saturated 0.5 M $H_2SO_4$ at different potential range.

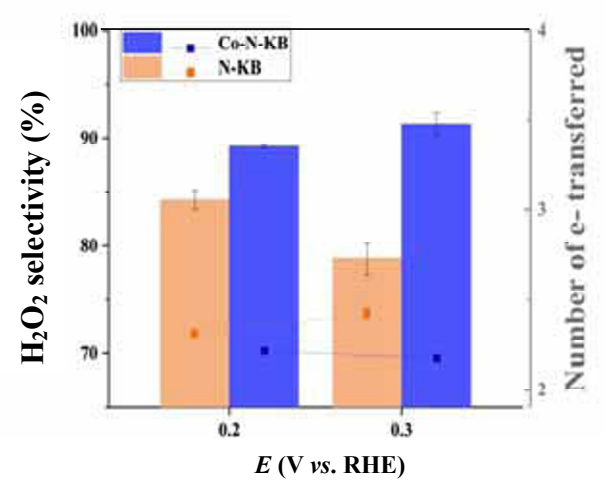


**Fig. 10.** $H_2O_2$ selectivity and the number of transferred electrons of N-KB and Co-N-KB catalysts with the same catalyst loading measured by RRDE with 1600 rpm in $O_2$ saturated 0.5 M $H_2SO_4$ at 0.2 and 0.3 $V_{RHE}$.

and transferred electron number for Co-N-KB and N-KB were evaluated in Fig. 10 at 0.2 and 0.3 $V_{RHE}$, where the Co function can be distinguished.

The N-KB samples showed the selectivity under 85% with transferred electron numbers close to 2.5. The N doping may play a critical role to promote the $H_2O_2$ generation in acidic mediums [38]. Furthermore, incorporating Co-into N-KB structure further enhanced the $H_2O_2$ selectivity (nearly 90%) with the transferred electron number slightly above 2. The increased activity and selectivity could be due to the formation of Co-$N_x$ active sites in the catalyst structure. This finding is consistent with the previous studies in which Co-$N_x$ active sites promote $H_2O_2$ generation in acidic solutions [39,40]. These results suggested that the synthesized Co-N-KB catalyst is a promising catalyst for promoting the two-electron pathway to $H_2O_2$ in acid solutions.

### *3.3.2. The effect of the encapsulated Co-NPs on $H_2O_2$ selectivity*

The role of the embedded core Co-NPs was investigated to examine whether the Co-NPs were able to improve the $H_2O_2$ selectivity. The Co-N-KB sample was treated with 0.5 M $HClO_4$ at 80 °C for 3 h to leach out most of Co-NPs. The TEM image (Fig. 11) shows that the acid-treatment washed most Co NPs aggregates except for a few remaining in the carbon structure. Next, a comparative analysis *via* RRDE was carried out to study the $H_2O_2$ selectivity pre and post the leaching process. Fig. 12 presents the $H_2O_2$ selectivity of (Co-N-KB) and (Acid-W/Co-N-KB) samples. It can be observed that the $H_2O_2$ selectivity was not significantly changed even after some of Co-NPs being removed with acid. In addition, an extra control RRDE measurements (Fig. 13) examined under the same experimental conditions showed similar oxygen reduction reaction activity was observed on N-KB and commercial Co-NPs with a mean particle size of ~28 nm which were physically supported on N-KB with loadings of 2 and 50 $\mu g_{Co}$ $cm^{-2}$.These findings indicated that the embedded Co-nanoparticles in the Co-N-KB matrix could have negligible activity toward the partial ORR to $H_2O_2$, suggesting that the stable Co-$N_x$ moieties may be primarily responsible for promoting the $H_2O_2$ selectivity in both untreated and acid-treated samples.

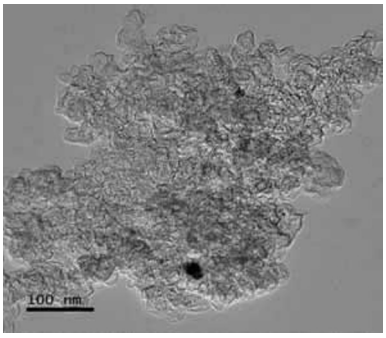


**Fig. 11.** TEM image of Acid-W/Co-N-KB sample.

### *3.3.3. $H_2O_2$ bulk electrolysis and durability*

The practical generation of $H_2O_2$ on the Co-N-KB was examined in an H-type electrolysis cell with an acidic electrolyte. Fig. 14 show the accumulated $H_2O_2$ amounts, and the $H_2O_2$ faradic efficiency (FE, %) of the Co-N-KB catalyst at applied potentials of 0.3 $V_{RHE}$ in $O_2$ saturated 0.5 M $H_2SO_4$ for 2 h tests. Remarkably, the catalyst achieved a high production rate of 100 mmol $g_{cat.}^{-1}$ $h^{-1}$ with $H_2O_2$ faradaic efficiency close to 85% at 0.3 $V_{RHE}$. Furthermore, catalyst durability was examined under the same conditions for 6 h at 2 h intervals. Based on the results, the catalyst had an almost consistent performance with a minimal decrease in the current, while the average faradic efficiency for the entire test period was nearly over 85%.

This outstanding performance was equivalent or slightly better than several of recorded the ORR carbon-based catalysts modified with N dopant and transition metals, suggesting that the Co-N-KB catalyst would be a great candidate to generate $H_2O_2$ for practical operations (Table 3).

### *3.4. The role of Co in enhancing $H_2O_2$ selectivity and generation*

The involvement of Co in promoting ORR to water or hy-

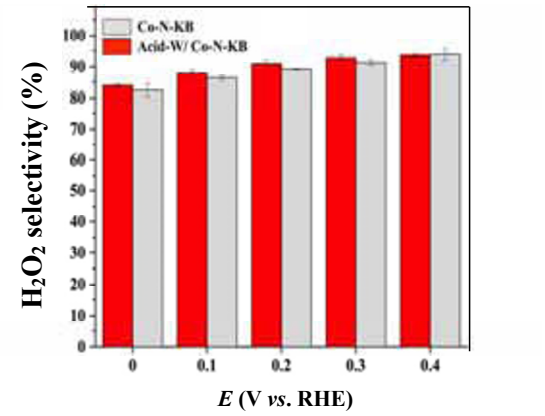


**Fig. 12.** $H_2O_2$ selectivity of Co-N-KB and Acid-W/Co-N-KB catalysts with the same catalyst loading measured by RRDE with 1600 rpm in $O_2$ saturated 0.5 M $H_2SO_4$.

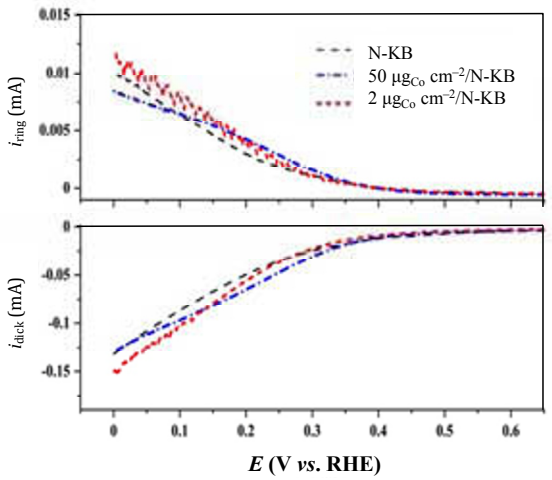


**Fig. 13.** Ring currents measured on the Pt-ring at 1.2 $V_{RHE}$ (top), the disk current (bottom) of N-KB, and commercial Co-NPs on N-KB with loading of 2 and 50 $\mu g_{Co}$ $cm^{-2}$ by RRDE at 1600 rpm in $O_2$ saturated 0.5 M $H_2SO_4$.

drogen peroxide remains a debate. Most of the published research has shown that Co-encapsulated nitrogen-doped carbon promotes ORR to water in alkaline solution [26,27,29]. It appeared that the synergic interaction between Co and N-dopants played a significant role in enhancing the catalytic activity of Co-N-C catalysts. However, the particular function of the various Co phases has not yet been fully understood. Furthermore, the size of the Co molecule is not as critical as the prominent Co phase developed in the carbon structure. Co-N-C catalysts have shown an improved four-electron ORR, with zero-valent Co being the most prominent Co phase. Besides, several Co- phases such as Co-$N_x$ could be formed that did not seem directly facilitating water formation as $Co^0$.

In the majority of cases, the Co-N-C promoting four-electron ORR was synthesized with a high Co loading. The addition of high quantities of Co could result in the development of several phases of Co, but more importantly, the $Co^0$ active sites could be increased, thereby benefiting the $4e^-$ pathway [27]. Low

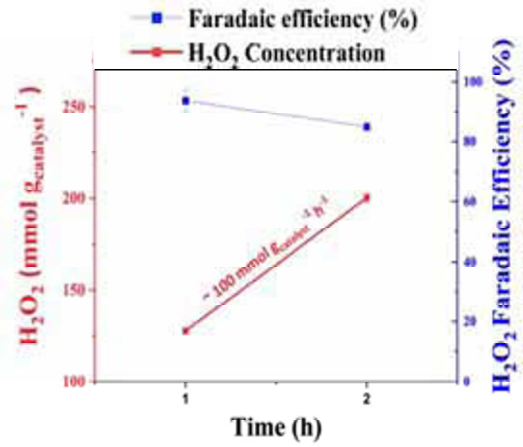


**Fig. 14.** $H_2O_2$ accumulated concentration standardized by catalyst loading over time (left) and $H_2O_2$ faradaic efficiency (right) of Co-N-KB catalyst in $O_2$ saturated 0.5 M $H_2SO_4$ at 0.3 $V_{RHE}$ with 250 rpm.

**Table 3**
Comparison of $H_2O_2$ production rate and faradic efficiency at acidic pH.

| Catalyst | pH | Potential ($V_{RHE}$) | $H_2O_2$ (mmol $g_{cat.}^{-1}$ $h^{-1}$) | $H_2O_2$ faradic efficiency (%) | Ref. |
|---|---|---|---|---|---|
| N-doped-CMK-3 | 0.3 | 0.2 | ~101.66 | ~73 | [38] |
| Co-N-C | 0.3 | 0.3 | ~84.2 | ~60 | [39] |
| Co-NC-im | 1 | 0.5 | ~49 | >95 | [37] |
| Co/carbon | 0 | 0.25 | ~5 | ~80 | [41] |
| Co-N-KB | 0.3 | 0.3 | ~100 | ~85 | This work |

Co-loading, on the other hand, showed a greater affinity for $H_2O_2$ generation, apparently because of very little to no $Co^0$ growth on the carbon surface, as shown in the study and in line with the other papers [37,39]. In this case, Co-$N_x$ could probably be the most prominent active site that can selectively reduce oxygen to $H_2O_2$.

It could be presumed that low Co loading has a slight or no contribution to $H_2O_2$ generation through ORR, and nitrogen-doped carbon is the actual active site. Here we hypothesized that Co-$N_x$ is the primary active site since the characterization techniques have shown the formation of Co-$N_x$ with few metallic Co residuals. Experimentally, the Co-N-KB was able to generate $H_2O_2$ at a very positive potential (0.5 $V_{RHE}$). In contrast, the N-KB sample did not experience ORR activity until the potential reached 0.2 $V_{RHE}$, mainly due to its high overpotential preventing $O_2$ from being reduced to $H_2O_2$. Moreover, the $H_2O_2$ bulk electrolysis at 0.3 $V_{RHE}$ on both Co-N-KB and N-KB (not shown) were tested, and the cobalt-doped sample produced 100 mmol $g_{cat.}^{-1}$ $h^{-1}$ while the N-KB was not able to generate $H_2O_2$ due to the potential limitation. This means that Co-$N_x$ might be the primary active site in the Co-N-KB catalyst, specifically at 0.3 $V_{RHE}$ or higher when N-dopants have no contribution on ORR. Furthermore, in a recent study, the role of Co-$N_x$ in promoting ORR to $H_2O_2$ has been analyzed by density functional theory (DFT). The study reported that Co-coordinated $N_x$ could facilitate the binding of $O_2$ disassociation product (*OOH) that will later be converted into $H_2O_2$. Additionally, the Co-$N_x$ sites exhibited faster kinetics for $H_2O_2$ dissociation than for the $H_2O_2$ decomposition to water [39].

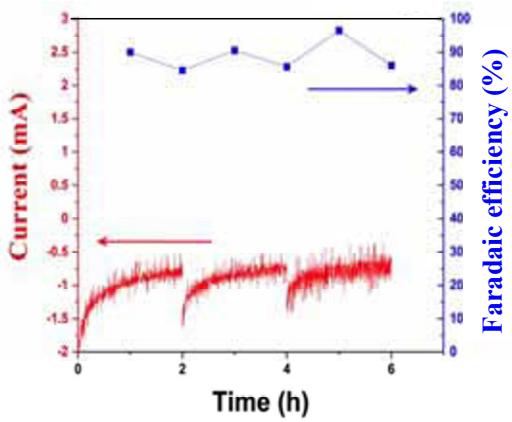


**Fig. 15.** Durability test: ORR reduction current (left) and $H_2O_2$ faradaic efficiency (right) of Co-N-KB catalyst in $O_2$ saturated 0.5 M $H_2SO_4$ at 0.3 $V_{RHE}$ with 250 rpm for 6 h.

## 4. Conclusions

We have demonstrated the successful synthesis of Co-N-KB with some catalytically active Co-$N_x$ sites using a facile and cost-effective method. Experimental findings showed that the formed Co-$N_x$ moieties within the Co-N-KB catalyst highly enhanced the electrocatalytic ORR activity towards $H_2O_2$ than those of non-metallic N-doped-KB. Under acidic conditions, the Co-N-KB showed a substantial increase in the peak current density of $O_2$ reduction, along with a significant shift of the onset potential toward the positive direction. Moreover, $H_2O_2$ selectivity of about 90% was observed at a broad potential range with the electron transfer number marginally above 2. Co-NPs showed similar activity towards partial ORR to $H_2O_2$ as the N-KB support, indicating that Co-$N_x$ was possibly the main active element. Furthermore, the catalyst long-term durability and its bulk $H_2O_2$ electrolysis confirmed the practical capability of Co-N-KB with an incredibly high $H_2O_2$ production rate of 100 mmol $g_{cat.}^{-1}$ $h^{-1}$ and enhanced $H_2O_2$ faradaic efficiency of 85% at 0.3 $V_{RHE}$. Accordingly, our material is a promising catalyst for the electrochemical reduction of $O_2$ that generates $H_2O_2$, and it likely could be incorporated into the cathode of more practical cells as a flow-cell electrolyzer, because carbon black has been widely used in fuel cell electrodes. The findings presented here significantly broaden the scope of carbon-based electrocatalyst synthesis with the correct set of features to promote the ORR two-electron pathway. Further studies are planned to study various aspects to enhance the current catalyst. The stated feasible synthesis procedure allowed us to integrate multiple heteroatom dopants, or metal oxides precursors, or change the catalyst structure to further increase the catalytic activity to $H_2O_2$ synthesis. Additional electrochemical measures such as pH effect and stability of the catalyst or electrolyzer design modification by means of introducing decoupled reactions will also be needed for a thorough understanding of the catalyst and its performance.

## Acknowledgments

B. Rawah would like to express his gratitude to Dapeng Jing for their assistance in XPS characterization and Warren Straszheim for SEM, and he also thanks to Carolina Selvati for helping out with XRD characterization. W. Li acknowledges his Richard Seagrave professorship for purchasing some materials and supplies.

## References

[1] X. Sheng, B. Wouters, T. Breugelmans, A. Hubin, I. F. Vankelecom, P. P. Pescarmona, *Appl. Catal. B*, **2014**, 147, 330–339.
[2] J. M. Campos-Martin, G. Blanco-Brieva, J. L. Fierro, *Angew. Chem. Int. Ed.*, **2006**, 45, 6962–6984.
[3] R. Arrigo, M. E. Schuster, S. Abate, G. Giorgianni, G. Centi, S. Perathoner, S. Wrabetz, V. Pfeifer, M. Antonietti, R. Schlögl, *ACS Catal.*, **2016**, 6, 6959–6966.
[4] J. S. Jirkovský, I. Panas, E. Ahlberg, M. Halasa, S. Romani, D. J. Schiffrin, *J. Am. Chem. Soc.*, **2011**, 133, 19432–19441.
[5] Y. J. Sa, C. Park, H. Y. Jeong, S. H. Park, Z. Lee, K. T. Kim, G. G. Park, S. H. Joo, *Angew. Chem. Int. Ed.*, **2014**, 53, 4102–4106.
[6] X. Sheng, N. Daems, B. Geboes, M. Kurttepeli, S. Bals, T. Breugelmans, A. Hubin, I. F. Vankelecom, P. P. Pescarmona, *Appl. Catal. B*, **2015**, 176, 212–224.
[7] I. Yamanaka, T. Onizawa, S. Takenaka, K. Otsuka, *Angew. Chem. Int. Ed.*, **2003**, 115, 3781–3783.
[8] A. Verdaguer-Casadevall, D. Deiana, M. Karamad, S. Siahrostami, P. Malacrida, T. W. Hansen, J. Rossmeisl, I. Chorkendorff, I. E. Stephens, *Nano lett.*, **2014**, 14, 1603–1608.
[9] S. Siahrostami, A. Verdaguer-Casadevall, M. Karamad, D. Deiana, P. Malacrida, B. Wickman, M. Escudero-Escribano, E. A. Paoli, R. Frydendal, T. W. Hansen, *Nat. Mater.*, **2013**, 12, 1137–1143.
[10] C. H. Choi, M. Kim, H. C. Kwon, S. J. Cho, S. Yun, H.-T. Kim, K. J. Mayrhofer, H. Kim, M. Choi, *Nat. Commun.*, **2016**, 7, 10922.
[11] Y. Sun, S. Li, Z. P. Jovanov, D. Bernsmeier, H. Wang, B. Paul, X. Wang, S. Kühl, P. Strasser, *ChemSusChem*, **2018**, 11, 3388–3395.
[12] J. Park, Y. Nabae, T. Hayakawa, M.-A. Kakimoto, *ACS Catal.*, **2014**, 4, 3749–3754.

### Graphical Abstract

*Chin. J. Catal.*, 2021, 42: 2296–2305 doi: 10.1016/S1872-2067(21)63804-4

**Electrocatalytic generation of hydrogen peroxide on cobalt nanoparticles embedded in nitrogen-doped carbon**

Basil Sabri Rawah, Wenzhen Li*
*Iowa State University, USA; University of Jeddah, Saudi Arabia*

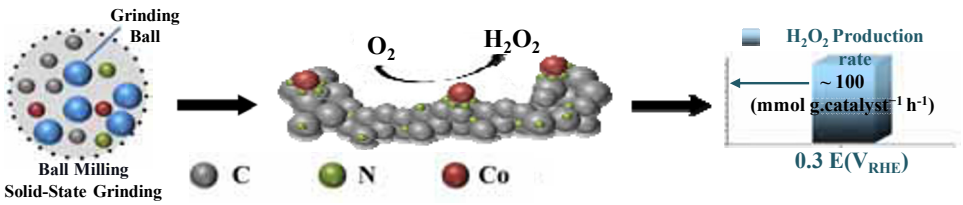


A straightforward milling technique was used to develop the cobalt nitrogen-doped carbon electrocatalyst consisting of a number of Co-$N_x$ moieties that selectively converted oxygen to hydrogen peroxide at a rate of 100 mmol $g_{cat.}^{-1}$ $h^{-1}$.

[13] D. Iglesias, A. Giuliani, M. Melchionna, S. Marchesan, A. Criado, L. Nasi, M. Bevilacqua, C. Tavagnacco, F. Vizza, M. Prato, *Chem*, **2018**, 4, 106–123.
[14] N. Daems, X. Sheng, I. F. Vankelecom, P. P. Pescarmona, *J. Mater. Chem. A*, **2014**, 2, 4085–4110.
[15] R. Cao, R. Thapa, H. Kim, X. Xu, M.G. Kim, Q. Li, N. Park, M. Liu, J. Cho, *Nat. Commun.*, **2013**, 4, 2076.
[16] G. Passard, D. K. Dogutan, M. Qiu, C. Costentin, D. G. Nocera, *ACS Catal.*, **2018**, 8, 8671–8679.
[17] C. Costentin, H. Dridi, J.-M. Savéant, *J. Am. Chem. Soc.*, **2015**, 137, 13535–13544.
[18] K. Mase, K. Ohkubo, S. Fukuzumi, *J. Am. Chem. Soc.*, **2013**, 135, 2800–2808.
[19] A. N. Oldacre, M. R. Crawley, A. E. Friedman, T. R. Cook, *Chem.-Eur. J.*, **2018**, 24, 10984–10987.
[20] P. Gouerec, M. Savy, *Electrochim. Acta*, **1999**, 44, 2653–2661.
[21] Z. S. Wu, L. Chen, J. Liu, K. Parvez, H. Liang, J. Shu, H. Sachdev, R. Graf, X. Feng, K. Müllen, *Adv. Mater.*, **2014**, 26, 1450–1455.
[22] S. Brüller, H.-W. Liang, U. I. Kramm, J. W. Krumpfer, X. Feng, K. Müllen, *J. Mater. Chem. A*, **2015**, 3, 23799–23808.
[23] K. Ghosh, M. Kumar, T. Maruyama, Y. Ando, *J. Mater. Chem.*, **2010**, 20, 4128–4134.
[24] N. Cai, S. Xia, X. Zhang, Z. Meng, P. Bartocci, F. Fantozzi, Y. Chen, H. Chen, P. T. Williams, H. Yang, *ChemSusChem*, **2020**, 13, 938–944.
[25] N. V. Klassen, D. Marchington, H. C. McGowan, *Anal. Chem.*, **1994**, 66, 2921–2925.
[26] Y. Liu, H. Jiang, Y. Zhu, X. Yang, C. Li, *J. Mater. Chem. A*, **2016**, 4, 1694–1701.
[27] Y. Su, Y. Zhu, H. Jiang, J. Shen, X. Yang, W. Zou, J. Chen, C. Li, *Nanoscale*, **2014**, 6, 15080–15089.
[28] Y. Qiu, J. Huo, F. Jia, B. H. Shanks, W. Li, *J. Mater. Chem. A*, **2016**, 4, 83–95.
[29] S. Dilpazir, H. He, Z. Li, M. Wang, P. Lu, R. Liu, Z. Xie, D. Gao, G. Zhang, *ACS Appl. Energy Mater.*, **2018**, 1, 3283–3291.
[30] W. Xiong, H. Li, H. You, M. Cao, R. Cao, *Natl. Sci. Rev.*, **2020**, 7, 609–619.
[31] W. Sun, L. Du, Q. Tan, J. Zhou, Y. Hu, C. Du, Y. Gao, G. Yin, *ACS Appl. Mater. Interfaces*, **2019**, 11, 41258–41266.
[32] H. C. Huang, I. Shown, S. T. Chang, H. C. Hsu, H. Y. Du, M. C. Kuo, K. T. Wong, S. F. Wang, C. H. Wang, L. C. Chen, K. H. Chen, *Adv. Funct. Mater.*, **2012**, 22, 3500–3508.
[33] W. Ju, A. Bagger, G.-P. Hao, A. S. Varela, I. Sinev, V. Bon, B. R. Cuenya, S. Kaskel, J. Rossmeisl, P. Strasser, *Nat. Commun.*, **2017**, 8, 944.
[34] S. Guo, S. Zhang, L. Wu, S. Sun, *Angew. Chem. Int. Ed.*, **2012**, 51, 11770–11773.
[35] S. Yang, A. Verdaguer-Casadevall, L. Arnarson, L. Silvioli, V. Čolić, R. Frydendal, J. Rossmeisl, I. Chorkendorff, I. E. L. Stephens, *ACS Catal.*, **2018**, 8, 4064–4081.
[36] L. Lai, J. R. Potts, D. Zhan, L. Wang, C. K. Poh, C. Tang, H. Gong, Z. Shen, J. Lin, R. S. Ruoff, *Energy Environ. Sci.*, **2012**, 5, 7936–7942.
[37] A. Lenarda, M. Bevilacqua, C. Tavagnacco, L. Nasi, A. Criado, F. Vizza, M. Melchionna, M. Prato, P. Fornasiero, *ChemSusChem*, **2019**, 12, 1664–1672.
[38] Y. Sun, I. Sinev, W. Ju, A. Bergmann, S. R. Dresp, S. Kühl, C. Spöri, H. Schmies, H. Wang, D. Bernsmeier, B. Paul, R. Schmack, R. Kraehnert, B. Roldan Cuenya, P. Strasser, *ACS Catal.*, **2018**, 8, 2844–2856.
[39] Y. Sun, L. Silvioli, N. R. Sahraie, W. Ju, J. Li, A. Zitolo, S. Li, A. Bagger, L. Arnarson, X. Wang, T. Moeller, D. Bernsmeier, J. Rossmeisl, F. Jaouen, P. Strasser, *J. Am. Chem. Soc.*, **2019**, 141, 12372–12381.
[40] I. Yamanaka, R. Ichihashi, T. Iwasaki, N. Nishimura, T. Murayama, W. Ueda, S. Takenaka, *Electrochim. Acta*, **2013**, 108, 321–329.
[41] A. Bonakdarpour, D. Esau, H. Cheng, A. Wang, E. Gyenge, D. P. Wilkinson, *Electrochim. Acta*, **2011**, 56, 9074–9081.

# 氮掺杂碳包埋钴纳米粒子电催化合成过氧化氢

Basil Sabri Rawah [a,b], 李文震 [a,*]
[a]爱荷华州立大学, 化学和生物工程系, 生物可再生能源研究实验室, 艾姆斯, 美国
[b]吉达大学化学与材料工程学院, 吉达, 沙特阿拉伯

**摘要**: 电催化还原氧是一种新兴的可持续生产过氧化氢($H_2O_2$)的合成技术, 寻找低成本、高活性和高选择性的电催化剂是该技术实际应用的关键. 钴氮掺杂的碳材料因含有钴氮(Co-$N_x$)催化活性位, 成为一类新兴的可促进$H_2O_2$电化学合成的材料.

本文采用低能耗干式球磨外加控制热解的方法来制备包含许多Co-$N_x$结构的钴氮掺杂碳材料. 该方法使用材料廉价, 即将醋酸钴、2-甲基咪唑和Ketjenblack EC-600JD高纯度且导电的碳黑分别作为金属、氮和碳的前体. 在酸性介质中的电化学测试结果表明, 该材料的氧还原反应电流密度明显增加, 同时起始电位向正方向移动. 该催化剂在较大电位范围内对$H_2O_2$的选择性约为90%. $H_2O_2$整体电解实验表明, $H_2O_2$产率达到100 mmol $g_{cat}^{-1}$ $h^{-1}$, $H_2O_2$法拉第效率达到85% (0.3 V *vs*. RHE条件下2 h). 耐久性测试(在0.3 V *vs*. RHE条件下6 h)表明, 催化剂表现出相对稳定的性能, 且在整个测试循环中, 法拉第效率达到约85%, 表明催化剂在实际应用中具有良好的耐久性. 催化剂表现出较高的电催化合成$H_2O_2$活性和选择性可能是由于形成了Co-$N_x$活性位, 以及酸性环境和应用电位等其它因素的影响.

**关键词**: 过氧化氢; 双电子氧还原; 碳催化剂; 电催化

**收稿日期**: 2021-01-14. **接受日期**: 2021-03-06. **上网时间**: 2021-09-10.
***通讯联系人**. **电话**: +1-515-294-4582; **电子信箱**: wzli@iastate.edu
**本文的电子版全文由**Elsevier出版社在ScienceDirect上出版(http://www.sciencedirect.com/journal/chinese-journal-of-catalysis).